

Dynamic arrest of adhesive hard rod dispersions

Ryan P. Murphy,¹ Harold W. Hatch,² Nathan A. Mahynski,² Vincent K. Shen,² and Norman J. Wagner¹

¹Center for Neutron Science and Department of Chemical and Biomolecular Engineering, University of Delaware Newark, Delaware 19716, USA

²Chemical Informatics Research Group, Chemical Sciences Division, National Institute of Standards and Technology Gaithersburg, Maryland 20899 – 83080, USA

(Dated: December 13, 2019)

ELECTRONIC SUPPLEMENTAL INFORMATION (ESI)

Commercial equipment and materials identified in this work does not imply recommendation or endorsement by the National Institute of Standards and Technology.

Sample preparation

Adhesive hard rods (AHR) were synthesized and characterized as described in previous work [1, 2]. Briefly, silica rods are grown to different lengths in a water-in-oil emulsion [3], rods are calcined to remove residual polymer, and an octadecyl-brush layer is grafted onto the silica surface [1]. The hydrophobic coating on the particle surface (≈ 1 chain nm^{-2}) enables suspension into organic solvents, such as cyclohexane and tetradecane. Variations of this general methodology can be extended to other silica-based particles with different shapes, dimensions, and polydispersity [2]. The diameter D , length L , and aspect ratio L/D of AHR samples are listed in Table I from SEM measurements [1].

TABLE I. AHR particle dimensions given as the mean and one standard deviation obtained from SEM [1].

Sample	Diameter (nm)	Length (nm)	Aspect Ratio, L/D
AR3	259 ± 37	700 ± 76	2.7 ± 0.3
AR4	258 ± 43	1099 ± 252	4.2 ± 0.7
AR6	252 ± 36	1502 ± 512	5.9 ± 1.6
AR7	298 ± 65	2019 ± 747	6.8 ± 2.1

AHR dispersions were prepared by drying the coated rods under a nitrogen stream and then by drying for 10 – 16 hours at 50 °C under vacuum. After drying, rods were immediately weighed and suspended in n-tetradecane at a specified volume fraction ϕ calculated by $\phi = m_p \rho_p^{-1} (m_p \rho_p^{-1} + m_s \rho_s^{-1})^{-1}$, where m_p and m_s are the measured particle and solvent mass, respectively, and $\rho_p = 1.95 \pm 0.03 \text{ g cm}^{-3}$ and $\rho_s = 0.76 \pm 0.01 \text{ g cm}^{-3}$ are their densities. The particle density is calculated by $\rho_p = (m_b \rho_b^{-1} + (1 - m_b) \rho_{SiO_2}^{-1})^{-1}$, where ρ_b is the assumed brush density (octadecane, 0.78 g cm^{-3}), and ρ_{SiO_2} is the measured amorphous skeletal density of silica rods (2.1 g cm^{-3}). The calculated particle density remained consistent for different aspect ratios due to small

variations in the brush mass fraction m_b (4% to 6% by mass) [1]. For reference, particle volume fractions of 0.11, 0.21, 0.31, 0.42, and 0.52 correspond to a mass fraction of 0.23, 0.41, 0.54, 0.65, and 0.73, respectively. The uncertainty in ϕ (± 0.01 to ± 0.03) was determined from the higher limit and lower limit of the effective coated particle density in suspension, where the higher density limit is 2.1 g mL^{-1} (silica core), and the lower density limit is 1.8 g mL^{-1} if solvent is able to swell into a specific pore volume of $\approx 0.05 \text{ mL g}^{-1}$.

Small-amplitude oscillatory shear rheology (SAOS)

For SAOS frequency sweeps, the critical gel transition temperature T_{gel} is defined using the Winter-Chambon criterion [4, 5], which defines the temperature at which the dynamic moduli are approximately equivalent and scale with frequency as $G'(\omega) \sim G''(\omega) \sim \omega^{0.5}$ over a broad frequency range, typically in the range $\omega \approx 1 \text{ rad s}^{-1}$ to 10 rad s^{-1} . The uncertainty in T_{gel} is defined by the smallest temperature increment measured (± 1 °C), which is shown as error bars in Fig. 2a of the main text.

For concentrations where $\phi > \phi_g$, the glass transition temperature T_g was defined when the dynamic moduli increased exponentially upon further decreasing T and the slope $\Delta G/\Delta T$ increases significantly. The uncertainty in T_g is defined by the smallest temperature increments performed for SAOS frequency sweeps (± 1.0 °C). This transition was interpreted as the repulsion-driven glass (RDG) to attraction-driven glass (ADG) transition since $G' > G''$ for all examined T and ω . In Fig. 1, the T -dependent storage modulus G' is shown at a fixed frequency $\omega = 6.3 \text{ rad s}^{-1}$ for sample AR4 and AR6 ($\phi = 0.42$, $\phi > \phi_g$). The black arrows indicate that the RDG-ADG transition temperature is defined as $T_g = 27 \pm 1$ °C for AR4 (blue circles) and $T_g = 29 \pm 1$ °C for AR6 (green triangles). Below T_g , G' and G'' increase exponentially with decreasing T . Above T_g , the dynamic moduli are nearly independent of T and are weakly dependent on ω , where $G'(\omega) > G''(\omega)$, $G'(\omega) \sim \omega^n$ and $n \approx 0$ to 0.2.

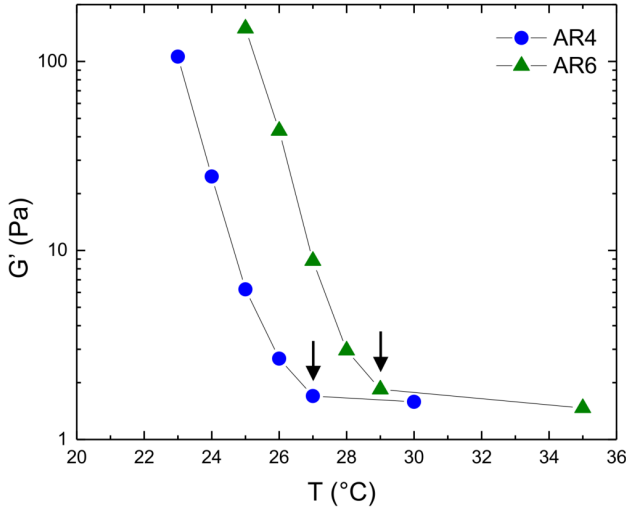


FIG. 1. Storage modulus G' at fixed frequency $\omega = 6.3 \text{ rad s}^{-1}$ as a function of temperature T when $\phi > \phi_g$. Sample AR4 (blue circles) and AR6 (green triangles) at $\phi = 0.42$. Black arrows indicate T_g at the point where a significant change in G' occurs. This point is defined as the RDG-ADG transition since $G' > G''$ at all examined T and ω . $T_g \approx 27^\circ\text{C}$ for AR4 and $T_g \approx 29^\circ\text{C}$ for AR6. Lines between symbols are shown as a guide.

Fiber-optic quasi-elastic light scattering (FOQELS)

Additional FOQELS measurements of AR4 at different ϕ and T are shown in Fig. 2 as colored symbols, and the fit to Eq. 1 in the main text is shown as solid black lines. Additional measurements for AR3, AR4, AR6, and AR7 are shown in Fig. 3.

FOQELS measurements for sample AR4 at $\phi = 0.21$ are shown in Fig. 4, where the autocorrelation functions have been normalized by β^{-2} such that $\beta^{-2}[g^{(2)}(t) - 1] \rightarrow 1$ as $t \rightarrow 0$ (refer to Eq. 1 in the main text). The data correspond to Fig. 2b in the main text are normalized and shown on a log-log scale (left) and log-lin scale (right). The signal to noise ratio decreases significantly for highly non-ergodic states ($T \ll T_{gel}$) and corresponds to a significant decrease in β . Note that sample vials were not rotated during the measurement. When the system becomes highly non-ergodic ($T \ll T_{gel}$), the parameters describing this non-ergodic state (β) will depend strongly on the particular speckle pattern that arrests within the scattering volume [6–8].

Ultra-small angle X-ray and neutron scattering (USAXS and USANS)

The slit-smearred USAXS and USANS data are compared in Fig. 5, where all USANS data are multiplied by the constant factor $30.61 = (\Delta q_{v,n}/\Delta q_{v,x})[(\rho_{p,x} -$

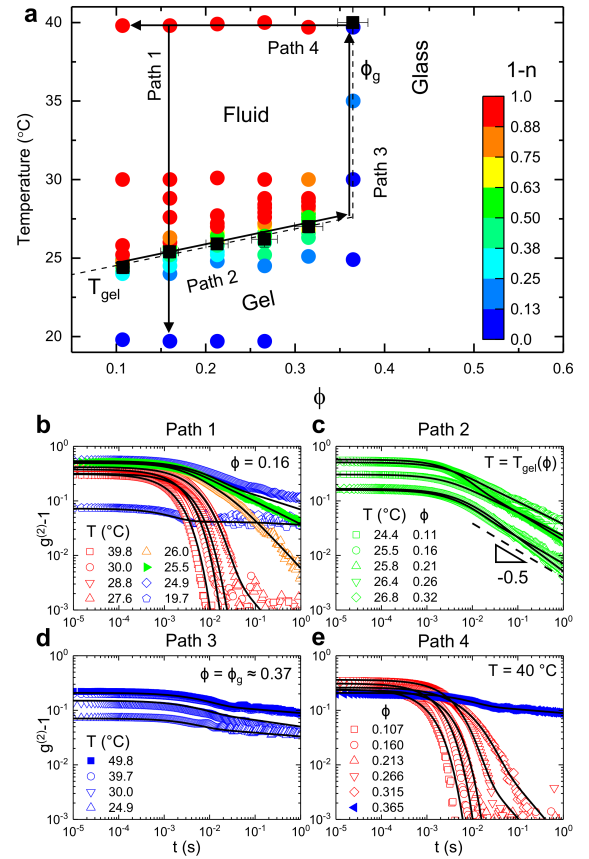


FIG. 2. (a) FOQELS map of the dynamic arrest transition of AR4 as a function of T and ϕ . Colors correspond to the best-fit power-law decay exponent n (Eq. 1 in main text) to FOQELS measurements. Red symbols corresponds to $n = 0$ ($1 - n = 1$) and fluid-like dynamics with a signal exponential decay of the autocorrelation function $g^{(2)} - 1$. Blue corresponds to $n = 1$ ($1 - n = 0$) and solid-like dynamics with no significant decay. Green corresponds to the critical criteria with $n = 0.5$ ($1 - n = 0.5$) which agrees with the frequency-dependent dynamic moduli measured with SAOS at the critical gel point. Arrows follow four different paths with varying T or ϕ . (b) Path 1 at fixed $\phi = 0.16$ transitions from the fluid-like to solid-like state with decreasing T (c) Path 2 at fixed $T = T_{gel}$ along the critical gel boundary where $n \approx 0.5$ (d) Path 3 along the glass boundary defined as $\phi = \phi_g = 0.37$ where the system remains arrested at all examined T . (e) Path 4 at fixed $T = 40^\circ\text{C}$ transitions from the solid-like to fluid-like state with decreasing ϕ , and also returning to the starting point of Path 1 in the fluid-like state.

$\rho_{s,x})/(\rho_{p,n} - \rho_{s,n})]^2$, where $\Delta q_{v,n}$ and $\Delta q_{v,x}$ are the respective slit lengths for USANS (0.117 \AA^{-1}) and USAXS (0.0282 \AA^{-1}), $\rho_{p,n}$ and $\rho_{p,x}$ are the particle scattering length densities for neutrons ($2.56 \times 10^{-6} \text{ \AA}^{-2}$) and X-rays ($1.56 \times 10^{-5} \text{ \AA}^{-2}$), $\rho_{s,n}$ and $\rho_{s,x}$ are the solvent scattering length densities for neutrons ($-4.44 \times 10^{-7} \text{ \AA}^{-2}$) and X-rays ($7.44 \times 10^{-6} \text{ \AA}^{-2}$). Scattering measurements using X-rays (USAXS and SAXS) and neutrons (USANS and SANS) are shown in Fig. 6 across the full range of ac-

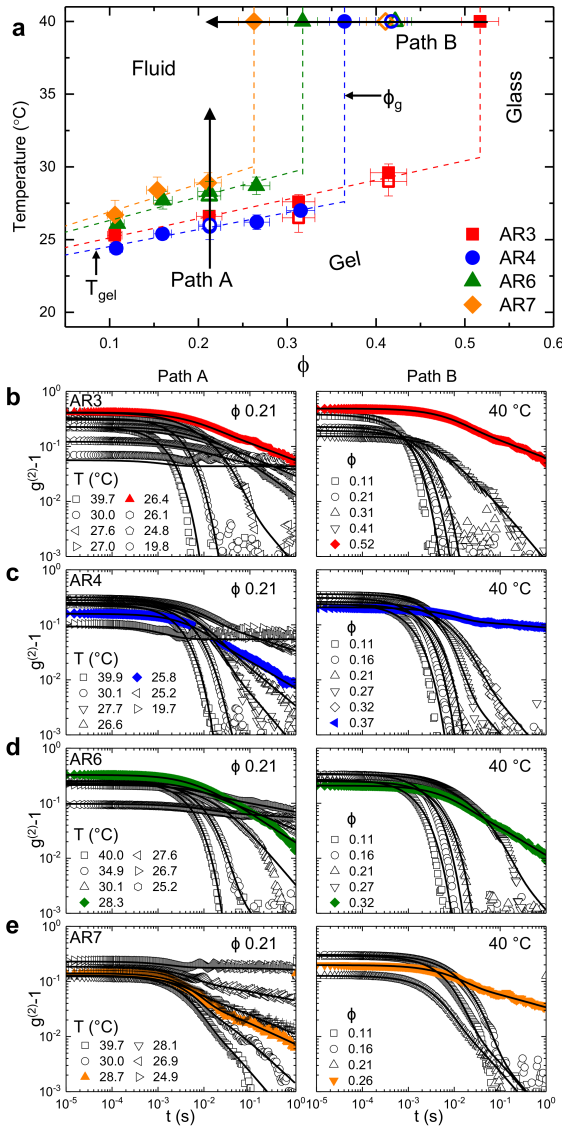


FIG. 3. (a) FOQELS map of the dynamic arrest transitions of AHR with different L/D as a function of T and ϕ . Closed symbols correspond to FOQELS measurements where $T = T_{gel}$ (slanted lines) or $\phi = \phi_g$ (vertical lines, see legend). Open symbols correspond to SAOS measurements. Arrows highlight shifts in the gel-like boundary at fixed $\phi \approx 0.21$ (Path A) and the repulsive glass-like boundary at fixed $T = 40^\circ\text{C}$ (Path B). (b-e) FOQELS measurements of the autocorrelation function $g^{(2)} - 1$ for AR3, AR4, AR6, and AR7 (top to bottom), in which the left and right columns corresponds to Path A and B, respectively.

cessible q . All USAXS measurements are shown in Fig. 7. All USANS measurements are shown Fig. 8.

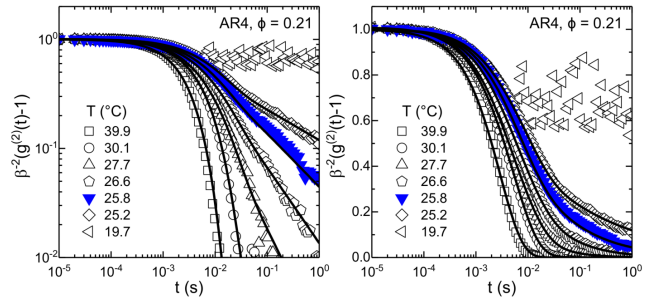


FIG. 4. Normalized FOQELS measurements for sample AR4 at $\phi = 0.21$, which have been normalized by β^{-2} to approach 1 in the limit that $t \rightarrow 0$. For comparison, symbols here correspond to the data shown in Fig. 2b (main text) on a normalized log-log scale (left) and log-lin scale (right). Solid lines correspond to model fits. Solid blue symbols correspond to the defined critical gel temperature $T_{gel} = 25.8 \pm 0.2^\circ\text{C}$.

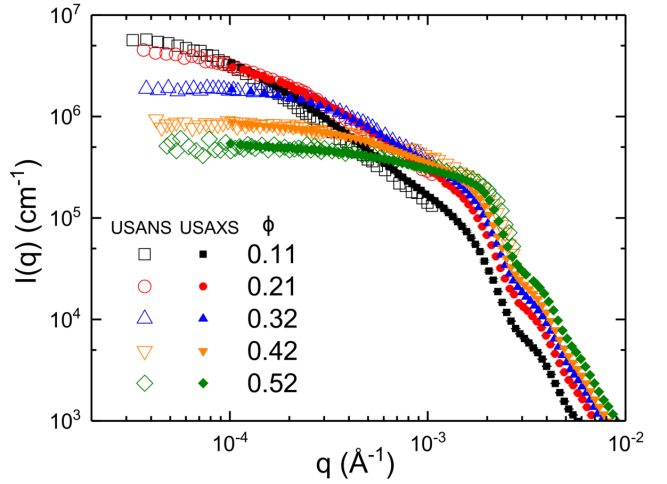


FIG. 5. Comparison of slit-smeared USAXS (solid symbols, 15°C) and USANS (open symbols, $15\text{--}27^\circ\text{C}$) on an absolute intensity scale. USANS data are vertically scaled by the constant 30.61 (see text) corresponding to different slit lengths and scattering length densities for X-ray and neutron scattering measurements.

Scattering model for rigid cylinders with short-range attractions

The scattered intensity $I(q)$ is related to two distinguishable contributions, the form factor $P(q)$ and the structure factor $S(q)$. The form factor describes the size and shape of particles, while the structure factor describes the relative location of particles distributed throughout the sample. For a homogeneous dispersion of monodisperse spheres, the scattered intensity is $I(q) = NP(q)S(q)$, where N is the number density of spheres. With the appropriate models from integral equation theories and closure relationships, the structure factor contribution can be linked to the interparticle pair potential

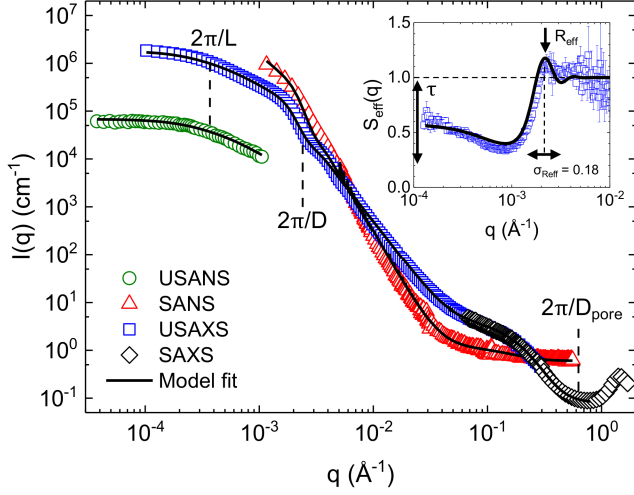


FIG. 6. The absolute scattering intensity $I(q)$ of sample AR4 at $\phi = 0.32$ and $T = 15^\circ\text{C}$ for different scattering methods defined in the legend. The model fit from Eq. 3 (black line) captures the measured $I(q)$ across the full range of q . The inset corresponds to the measured effective structure factor contribution $S_{eff}(q)$ (symbols), which is fit to the Baxter sticky hard sphere structure factor model (black line).[9] The τ parameter mainly affects the low- q region and compressibility as $q \rightarrow 0$, while the R_{eff} (σ_{Reff}) mainly affects the position (width) of the first primary peak. Note that X-ray data (USAXS and SAXS) and neutron data (USANS) are slit-smear data, while the SANS data is pinhole-smear data, both of which are accounted for in the scattering model and SasView fitting software.[10]

to extract quantitative information of interparticle interactions.

Interpreting the scattered intensity from a concentrated dispersion of anisotropic particles is less trivial. However, here a simple model is proposed to decouple the particle form factor and structure factor, which coincidentally follows the rigid particle approximation proposed in the framework of reference interaction site models (RISM) [11–14]. In the RISM framework, anisotropic particles are defined by a collection of smaller symmetric interaction sites. Each site is rigidly linked to other sites within the same particle, which is defined by the site-site (ss) *intraparticle* structure factor $\omega_{ss}(q)$. For sites i and j arranged in a straight line of length L and site spacing D , $\omega_{ss}(q) = (N)^{-1} \sum_{i,j=1}^N (|i-j|qD)^{-1} \sin(|i-j|qD)$ [13, 15]. N is the number of sites per particle, or equivalently $N = L/D$ when L/D is an integer. Sites between neighboring particles can interact based on their pairwise interaction potential, which is defined by the site-site *interparticle* structure factor $S_{ss}(q)$. Written in the site-site reference frame, the total scattered intensity $I(q)$ for monodisperse sites is given similarly to monodisperse spheres as [13]

$$I(q) = N_s P_{ss}(q) S_{ss}(q) \quad (1)$$

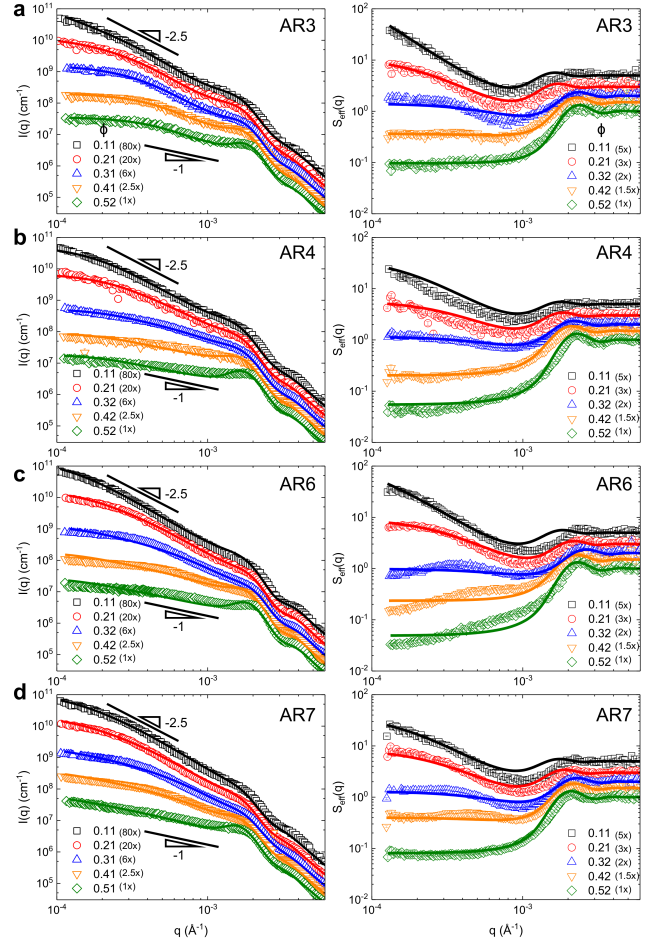


FIG. 7. (a-d) Desmeared USAXS measurements of AR3, AR4, AR6, and AR7 (top to bottom) in the solid-like state at $T = 15^\circ\text{C}$ (left column). Fits to the scattering model in Eq. 3 (Eq. 2 in main text) are shown as colored lines. The corresponding effective structure factor contribution $S_{eff}(q)$ (symbols) and fits to the Baxter sticky hard sphere structure factor (lines) are shown in the right column. Core volume fractions are defined in the figure legends. For clarity, $I(q)$ and $S_{eff}(q)$ measurements are vertically shifted by factors defined in the figure legend.

where N_s is the number density of sites, and $P_{ss}(q)$ is the form factor (shape) of an indistinguishable site.

To describe Eq. 1 in terms of the particle center-of-mass (cm) reference frame, the rigid particle approximation is employed, given as [13–16]

$$S_{ss}(q) \cong \omega_{ss}(q) S_{cm}(q) \quad (2)$$

in which $S_{cm}(q)$ is the center-of-mass structure factor. In this approximation, it is assumed that interaction sites are indistinguishable, particles retain an isotropic distribution, particles acquire an effective isotropic density profile, and particles do not deform or rotate. In other words, particles are assumed to behave as an effective spherical cloud of interaction sites. This approximation

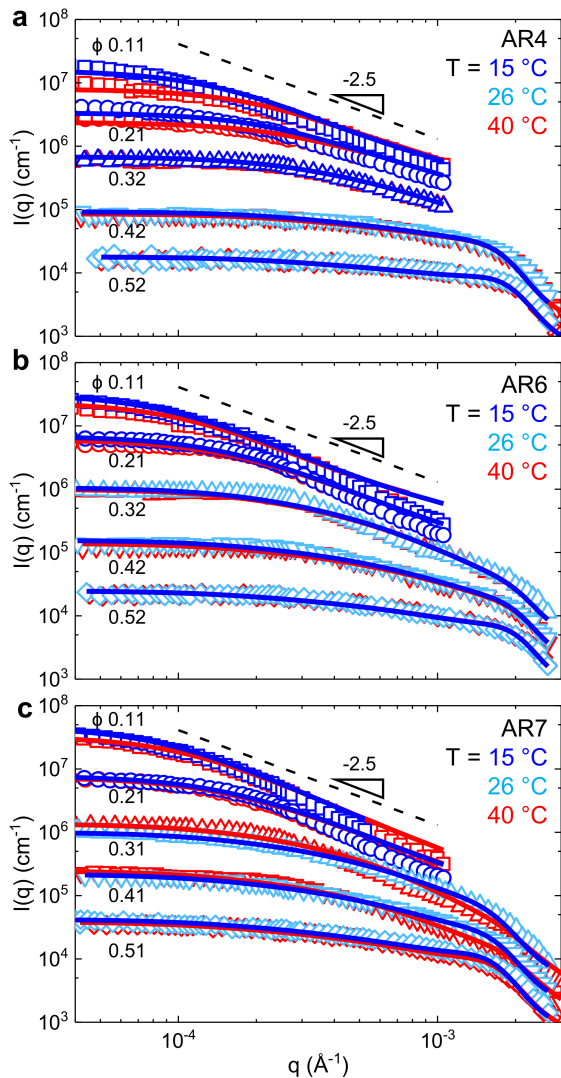


FIG. 8. (a-c) Slit-smear USANS measurements of AR4, AR6, and AR7 (top to bottom) at $T = T_{low}$ (blue symbols, 15 °C or 26 °C) and at $T = T_{high}$ (red symbols, 40 °C). Core volume fractions are defined in the figure. For clarity, $I(q)$ measurements are vertically shifted by factors 100, 30, 10, 3, and 1 (top to bottom). Solid red lines correspond to the model fit (Eq. 3) at $T_{high} = 40$ °C, and solid blue lines correspond to model fit at either $T_{low} = 15$ °C or 26 °C.

was also proposed in mode-coupling simulations of various concentrated anisotropic particles [13–19].

Rearrangements to Eq. 1 are made with the rigid particle approximation in Eq. 2 and the substitution $N_s \omega_{ss}(q) P_{ss}(q) = N_{cyl} P_{cyl}(q)$. The latter substitution conserves total particle volume fraction ϕ , in which $P_{ss}(q)$ is a cylindrical site form factor with $L/D = 1$, N_{cyl} is the number density of cylinders, and $P_{cyl}(q)$ is the cylinder form factor (solid lines in Fig. 1 in main text). Note that using orientation-averaged cylindrical sites, instead of spherical sites, is a good approximation only at lower q ($q < 2\pi D^{-1}$) and introduces subtle error

at higher q that correspond to differences in scattering from the site surface [20]. Within the particle center-of-mass reference frame, the total scattered intensity is approximated as

$$I(q) \cong N_{cyl} P_{cyl}(q) S_{cm}(q) \quad (3)$$

where $S_{cm}(q)$ is the isotropic center-of-mass structure factor of interest. Eq. 3 (Eq. 2 main text) is fit to the measured $I(q)$ using SasView software [10] with additional integration to account for polydispersity in cylinder radius R and length L , as described below.

The orientation-averaged form factor was fit with a polydisperse cylinder model $P_{cyl}(q)$ given by [10]

$$P_{cyl}(q) = \frac{1}{V_{avg}} \int \int \int [F_{cyl}(q, \alpha)]^2 f(R) f(L) \sin \alpha \, d\alpha \, dR \, dL \quad (4)$$

with

$$F_{cyl}(q, \alpha) = 2(\Delta\rho)(\pi R^2 L) \frac{\sin(\frac{1}{2}qL \cos \alpha)}{\frac{1}{2}qL \cos \alpha} \frac{J_1(qR \sin \alpha)}{qR \sin \alpha} \quad (5)$$

and a Schulz distribution in the cylinder radius R and length L ,

$$f(x) = \frac{1}{A} (z+1)^{z+1} \left(\frac{x}{\bar{x}}\right)^z \exp\left(\frac{-(z+1)x/\bar{x}}{\bar{x} \Gamma(z+1)}\right) \quad (6)$$

where V_{avg} is the average particle volume, $\Delta\rho = \rho_p - \rho_s$ is the scattering length density (SLD) difference between the particle and solvent, α is the angle between the scattering wavevector q and the cylinder length axis, J_1 is the first order Bessel function, z is a parameter given by the standard deviation σ_x and mean \bar{x} with $z = (1-p)^2/(p)^2$, $p = \sigma_x/\bar{x}$ (standard deviation and mean of x), and A is a normalization constant to ensure the function integrates to unity [10].

The center-of-mass structure factor $S_{cm}(q)$ was fit with the analytical form of the Baxter sticky hard sphere structure factor model [9, 21, 22], as implemented in SasView v4.1.2 [10], which uses the Ornstein-Zernike integral equation and the Percus-Yevick closure relationship to relate the interparticle pair potential, radial distribution function, and the structure factor. The reduced temperature τ , or Baxter sticky parameter, is defined as [9, 10]

$$\tau = \frac{1}{12\delta} \exp(-U_0/k_B T) \quad (7)$$

where the perturbation distance parameter is $\delta = \Delta/(D_{eff} + \Delta)$, Δ is the distance of short-range attraction, $D_{eff} (= 2R_{eff})$ is the effective interaction diameter, and U_0 is the attraction potential energy. Decreasing τ corresponds to increasing attraction strength or stickiness. From the extended theory of corresponding states

[23–25], when the range of attraction is small relative to the core diameter, τ can be related to the reduced second virial coefficient B_2^* by equating through square-well potential, giving

$$B_2^* = 1 - (4\tau)^{-1} \quad (8)$$

in which $B_2^* = B_2/B_2^{HS}$, B_2 is the (temperature-dependent) second virial coefficient, and B_2^{HS} is the (athermal) second virial coefficient for a hard sphere. For a hard sphere system, B_2^{HS} must be positive since $B_2^{HS} = (2/3)\pi D^3 = 4V_c$, in which D is the hard core diameter and V_c is the hard core volume. For a system of adhesive hard rods, conditions where $B_2^* < 1$ ($B_2^* > 1$) correspond to net-attractive (net-repulsive) interactions relative to a hard sphere system at equivalent interaction volume fraction η , in which $\eta = \phi(1 - \delta)^{-3}$. The special condition in which $B_2^* = 0$ is the Boyle temperature, where the ensemble-averaged attractions and repulsions negate each other, and the system behaves as an ideal gas.

Model fitting procedure

The scattering model given in Eq. 3 (Eq. 2 in the main text) can be easily reproduced using SasView software [10]. After loading SasView, use the multiplication function (Fitting, Add/Multiply Models) to multiply a cylinder form factor model (model1 = cylinder) and the sticky hard sphere structure factor (model2 = stickyhard-sphere). The cylinder form factor in SasView employs the above Eq. 4 and Eq. 5, as well as Schulz distributions to account for polydispersity in D and L using Eq. 6. The sticky hard sphere structure factor is the analytical form proposed by Menon *et al.* [9].

The only two freely fitting parameters in the scattering model include (1) the reduced temperature τ and (2) the effective interaction radius R_{eff} . All other pre-determined and unknown parameters are fixed as discussed below. Pre-determined model parameters include (1) the core volume fractions ϕ and (2) the cylinder form factor parameters D , σ_D , L , and σ_L , which are based on the fit to P_{cyl} at dilute concentrations. The best fit parameters to $P_{cyl}(q)$ are given in Tab. II, which corresponds to the solid lines shown in Fig. 1 of the main text. Scattering at high q ($> 0.01 \text{ \AA}^{-1}$, Fig. 6) corresponded to the internal pore structure of rods. The rod dimensions were significantly larger than internal pores, such that internal pores decreased the effective particle SLD in the lower q -range of interest ($q < 0.01 \text{ \AA}^{-1}$). The internal porosity ($\approx 20\%$) gave an effective particle SLD of $2.56 \times 10^{-6} \text{ \AA}^{-2}$ and $1.56 \times 10^{-5} \text{ \AA}^{-2}$ for neutron and x-ray scattering, respectively. The particle form factors were measured for calcined silica rods suspended in ethanol under dilute conditions ($\phi \approx 0.002$), where interparticle interactions were negligible and $S_{cm}(q) \approx 1$.

TABLE II. USAXS fit parameters using the polydisperse cylinder form factor model $P_{cyl}(q)$. Parameters include scale or volume fraction (ϕ), cylinder radius ($R = D/2$), polydispersity in radius ($PD = \sigma_R/R$), and cylinder length (L). Fixed parameters include the incoherent scattering background (B), the effective particle SLD (ρ_p), the solvent SLD (ρ_s), and polydispersity in length (σ_L/L).

Parameter	AR3	AR4	AR6	AR7
Scale (ϕ)	2.38E-03	2.38E-03	2.41E-03	2.23E-03
B (cm^{-1})	0.12	0.12	0.12	0.12
ρ_p (\AA^{-2})	1.56E-05	1.56E-05	1.56E-05	1.56E-05
ρ_s (\AA^{-2})	7.44E-06	7.44E-06	7.44E-06	7.44E-06
R (\AA)	1292	1306	1275	1428
σ_R/R	0.262	0.252	0.214	0.258
L (\AA)	10224	17018	22955	28356
σ_L/L	0.11	0.23	0.34	0.37

The other unknown model parameters include (1) the reduced short-range attraction distance δ and (2) the polydispersity in the effective interaction radius $PD_{Reff} = \sigma_{Reff}/R_{eff}$. The short-range perturbation distance $\delta = 0.01$ was fixed based on approximate brush distances ($\approx 3 \text{ nm}$) and rod diameters ($\approx 300 \text{ nm}$). Smaller δ (< 0.01) produces negligible change in τ and R_{eff} . Moreover, equivalent τ values are obtained at equivalent interaction volume fractions $\eta = \phi(1 - \delta)^{-3}$, which accounts for systems with different δ [9]. Meanwhile, PD_{Reff} was determined empirically to be ≈ 0.18 by minimizing the model error for all scattering measurements and for all conditions of L/D , ϕ , and T . The empirical condition $PD_{Reff} = 0.18$ was similar to the rod diameter polydispersity ($\sigma_D/D \approx 0.2 - 0.3$), and it was consistent for both neutron and X-ray scattering measurements. The unknown parameters $\delta = 0.01$ and $PD_{Reff} = 0.18$ were fixed in all model fits to best evaluate the τ parameter of interest.

The effective structure factor contribution, $S_{eff}(q) = I(q)/(P(q)N_{cyl})$ was obtained from desmeared USAXS curves using the Indra software package [26–28]. Consistent values of τ and R_{eff} were also obtained from fitting only the contribution of $S_{eff}(q)$ to the Baxter model [9], as shown in Fig. S7. Error minimization routines between the model and measurements were performed using SasView v4.1.2 [10]. In all analysis routines, the particle anisotropy is important and accounted by averaging the scattered intensity over all particle orientations. Shape anisotropy is accounted for in the orientation-averaging of $P_{cyl}(q)$ (solid lines in Fig. 1 main text), and it is inherent within the measured form factor $P(q)$ (symbols in Fig. 1 main text). The measured particle form factor $P(q)$ appears in the calculation of $S_{eff}(q) = I(q)/(P(q)N_{cyl})$, which accounts for the shape anisotropy in $S_{eff}(q)$.

Model parameter sensitivity

The error in τ corresponds to the systematic error obtained from repeated measurements and fitting trials, which employed both neutron scattering neutron and X-ray scattering methods. For all samples, the standard deviation in τ was relatively small ($< 10\%$) when $\phi < 0.3$, but variations increased considerably when $\phi > 0.3$. This larger variation in τ was speculated to occur from competing aging effects between liquid crystal formation and glass formation at higher ϕ .

The parameter R_{eff} was found to decrease within the range between ≈ 230 nm to ≈ 150 nm with increasing ϕ . Importantly, these variations in R_{eff} did not significantly affect the τ fit at low- q . In Fig. 9, example perturbations in all model fitting parameters (a) τ at fixed R_{eff} and (b) R_{eff} at fixed τ are shown for sample AR4 at different ϕ (top to bottom, $\phi = 0.11, 0.32$, and 0.52). This sensitivity analysis demonstrates that the uncertainty in R_{eff} is greater at lower ϕ , while the uncertainty in τ is greater at higher ϕ .

In Fig. 9c, different constraints to the effective interaction radius R_{eff} are also compared. As demonstrated for a wide range of ϕ , the unconstrained fit to R_{eff} (177 nm $< R_{eff} < 213$ nm, best fit, black lines) produced a nearly indistinguishable fit when compared to the constrained fit ($R_{eff} = 177$ nm, green lines). If the constraint $R_{eff} = R$ was employed (orange lines), then there is discrepancy between the model fit and measurements at intermediate q where $q \approx \pi/R_{eff}$. However, notice that variations in R_{eff} or the polydispersity in R_{eff} (pink lines) do not significantly influence the lowest q -range, which is mainly sensitive to τ at a given concentration. Consequently, the dimensionless state diagram shown in Fig. 4a of the main text does not change significantly with the fitting constraints imposed on the unknown effective interaction radius R_{eff} .

When fitting $I(q)$ obtained from simulations, the conditions $R_{eff} = D/2$, $\Delta = 2R_g = 0.08D$, and $\delta = 0.074$ were used. Similar to the analysis of experimental data, physically relevant variation of R_{eff} did not significantly affect the fit at low- q . As demonstrated in Fig. 10, simulations of bidispersed cylinders confirmed that τ and $S(q \rightarrow 0)$ do not change significantly after explicitly adding polydispersity in D , L , or δ .

We suspect the apparent discrepancy in the best-fit effective radius for simulations ($R_{eff} = R$) and experiments ($R_{eff} \approx 1.3R$ to $\approx 2R$) occurs from neglecting relevant forces in simulations. For example, simulations do not consider interparticle friction and hydrodynamic interactions between rods, which may produce a different average center-of-mass distance (R_{eff}) at the dynamic arrest transition. Nevertheless, this apparent discrepancy in R_{eff} between simulation and experiment does not influence the reported effective interaction strength

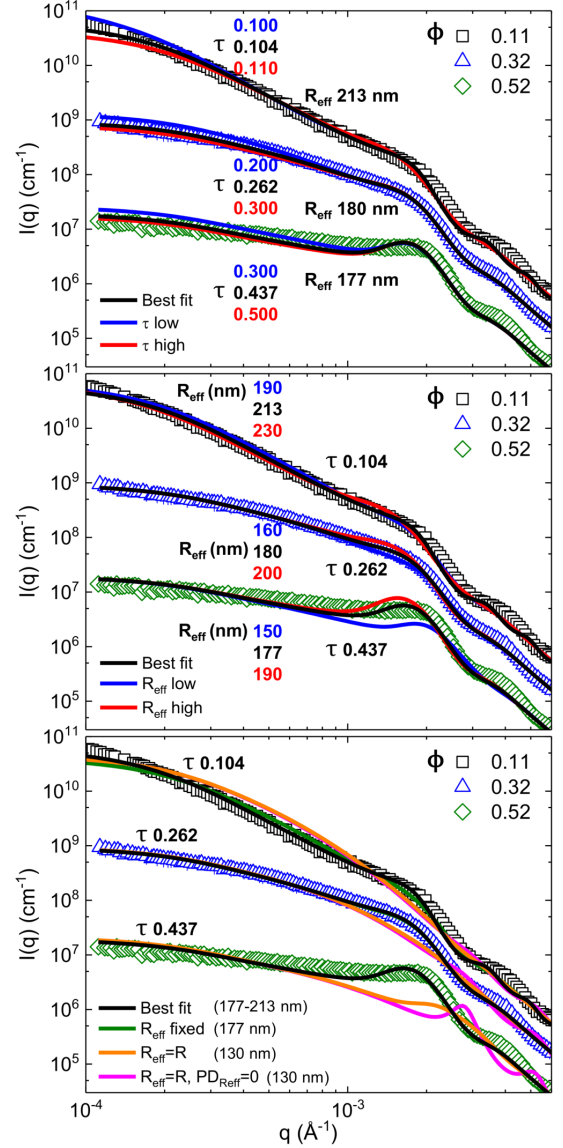


FIG. 9. Measured desmeared USAXS intensities for sample AR4 at 15°C and three different ϕ (symbols, top to bottom, $0.11, 0.32$, and 0.52), which are vertically shifted for clarity. For comparison, the same measured $I(q)$ (symbols) and best fits (black lines) are shown in each panel. The two key unknown parameters in the model are the effective interaction radius R_{eff} and the reduced temperature τ . Solids lines show the applied model fits to Eq. 3 at (a) fixed R_{eff} with varying τ , and (b) fixed τ with varying R_{eff} . Perturbations of the fit parameters in (a) and (b) correspond to lower values (blue), higher values (red), and at the best fit value (black) values shown in the panel [20]. (c) Additional constraints in the unknown hard sphere interaction radius R_{eff} are compared with fixed R_{eff} (green, 177 nm, $PD_{R_{eff}} = 0.18$), with the constraint $R_{eff} = R$ (orange, 130 nm), and with no polydispersity and $R_{eff} = R$ (pink, 130 nm, $PD_{R_{eff}} = 0$). Although variations do occur near $q \approx \pi/R_{eff}$, no significant variations in the low- q region, which remain sensitive primarily to τ at a given η .

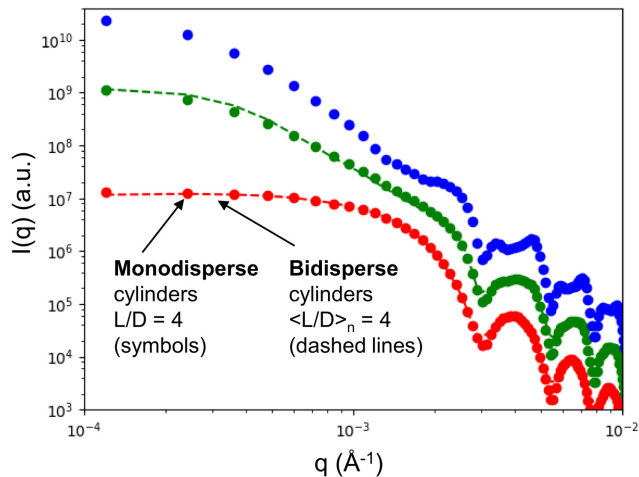


FIG. 10. MC simulations are performed for cylinders with orientation-dependent attractions and hard-core repulsions [29, 30]. The orientation-averaged scattered intensity $I(q)$ for monodisperse cylinders at $\phi = 0.11$ ($\eta = 0.14$) is shown as closed symbols, while $I(q)$ for bidispersed cylinders is shown as dashed lines. Symbol and dashed line colors correspond to different attraction strengths or potential well-depths, given as $\epsilon = 0.32$ (red), $\epsilon = 15.44$ (green), and $\epsilon = 63.44$ (blue). Polydispersity is defined as the ratio of the standard deviation and mean. For the monodisperse system, $PD = 0$ for all parameters. For the bidispersed system, $PD_L = 10\%$ for cylinder core length L , $PD_D = 5\%$ for cylinder core diameter D , and $PD_\delta = 5\%$ for the reduced attraction distance $\delta = \Delta/(D + \Delta)$. The monodisperse and bidispersed systems of cylinders with orientation-dependent attractions can be described by an effective isotropic potential with short-range attractions, as characterized by a reduced temperature τ . Data are vertically shifted for clarity.

τ at the gel boundary (Fig. 4a of the main text) or the glass volume fraction ϕ_g at the glass boundary (Fig. 4b of the main text). Although the simulations are limited to lower core volume fractions $\phi < 0.2$, experiments suggest the rigid particle approximation and scattering model (Eq. 2 from the main text) is suitable for concentrated AHR dispersions up to $\phi \approx 0.52$ and $L/D \approx 7$.

Dimensionless state diagram

When $\delta \leq 0.01$, variations in δ have negligible effect on τ and R_{eff} . However, when approximately $0.03 \leq \delta \leq 0.1$, the sensitivity to δ can be significant when comparing results in the $\tau - \phi$ plane, even when attraction distances are relatively short-ranged ($\leq 10\% D$). This δ -dependence emerges from the perturbation solution to the Baxter sticky hard sphere model proposed by Menon *et al.* [9]. This solution considers the *interaction* volume fraction η instead of the core volume fraction ϕ , in which $\eta = N\pi a^3/6$, N is the number density, a is the interaction diameter $a = D + \Delta$, D is the hard core

diameter, and Δ is the short-range interaction distance. The perturbation parameter, $\delta = \Delta/a = \Delta/(D + \Delta)$, ranges from 0 to 1 in the limit that Δ ranges from 0 to ∞ , respectively. The relationship between the core volume fraction ϕ and the interaction volume fraction η is given by $\eta = \phi(1 - \delta)^{-3}$ [9]. If δ resides within approximately $0.03 \leq \delta \leq 0.1$, then the distinction between η and ϕ becomes significant.

By comparing τ as a function of η , as opposed to the core volume fraction ϕ , the somewhat arbitrary choice of δ is accounted for between different systems. Consequently, the $\tau - \eta$ plane provides a more suitable comparison between systems with different δ , provided that the attraction range remains small compared to the diameter ($\Delta \ll D$). The τ values shown Fig. 4a in the main text are re-scaled in Fig. 11 as a function of the core volume fraction ϕ using the conversion $\eta = \phi(1 - \delta)^{-3}$. The difference between ϕ and η is negligible when $\delta \leq 0.01$ (δ listed in the caption). However, the conversion between ϕ and η is significant when approximately $\delta > 0.03$. Given that $\delta = 0.074$ in simulations, the AHR simulations demonstrate better agreement with AHR experiments and previous AHS measurements in the $\tau - \eta$ plane. Thus, the systematically higher τ obtained from AHR simulations is attributed to differences in δ when compared in the $\tau - \phi$ plane.

The reduced second virial coefficient B_2^* is related to the reduced temperature τ by Eq. 8 [23]. For comparison, the results from Fig. 4a of the main text are also shown in the $B_2^* - \eta$ plane in Fig. 11b. Refer to the caption for the symbol notation and δ values. The conditions $B_2^* < 1$ occur for all η and L/D , which corresponds to net-attractive interactions relative to perfect hard sphere behavior. The convergence of B_2^* at lower $\eta < 0.2$ is also evident for AHR experiments and simulations at different L/D . For simulated systems at the rigidity percolation criterion $\langle n_c \rangle \approx 2.4$, the results for AHR simulations show good agreement with AHS simulations [32], despite differences in the interaction potentials and δ parameters.

Particle volume dependence

Previous measurements of adhesive hard spheres revealed an apparent correlation between particle size and τ [24, 25, 31]. This particle size dependence was attributed to the effects of gravity, where gravity tends to increase the attraction strength (decrease τ) with increasing particle size [31].

To compare the particle size dependence for spheres and rods, the average particle volume V_p and the corresponding τ are shown in Fig. 12 at various ϕ . Different ranges of ϕ are shown by black squares ($\phi = 0.10 - 0.12$), red circles ($0.21 - 0.25$), blue upward triangles ($0.30 - 0.34$), orange downward triangles ($0.41 - 0.43$), and green diamonds ($0.50 - 0.52$). The solid lines shown

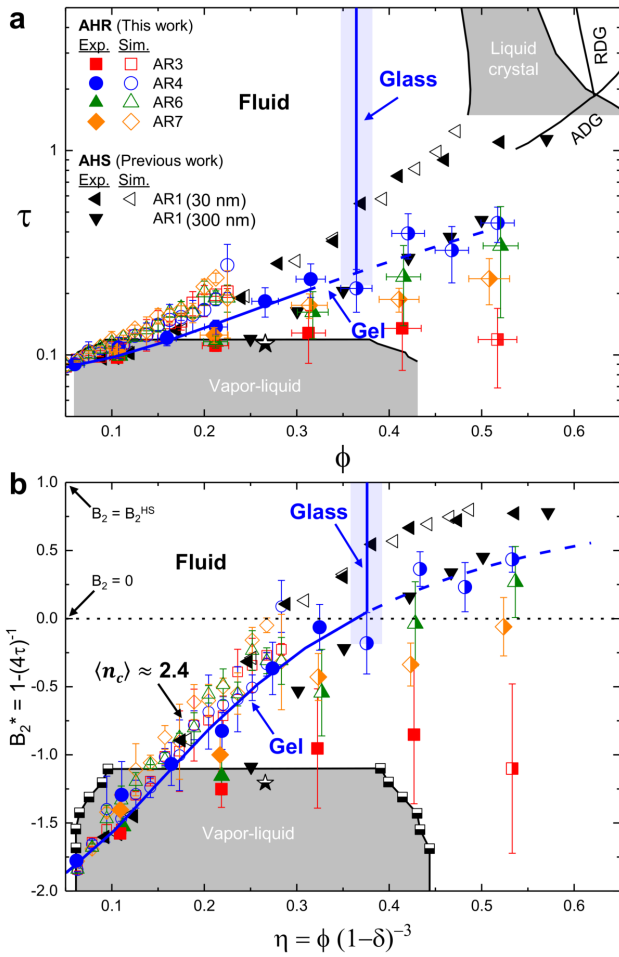


FIG. 11. Data from Fig. 4a of the main text are shown in the $\tau - \phi$ plane, where $\phi = \eta(1 - \delta)^3$. The δ values for different systems include: AHS experiments, 30 nm AR1, $\delta = 0.01$ (left triangles) [24, 25]; 300 nm AR1, $\delta = 0.001$ (down triangles) [31]; AHS simulations, $\delta = 0.01$ for the rigidity percolation criterion $\langle n_c \rangle \approx 2.4$ (open left triangles) and vapor-liquid binodal (bottom gray area) [32]; AHR simulations, $\delta = 0.074$ (this work); and AHR experiments, $\delta = 0.01$ (this work). Right-filled symbols correspond to AHR experiments in the glassy state where $\phi \geq \phi_g$. The case $\eta = \phi$ ($\delta \rightarrow 0$) is used for the AHS critical point (bottom-filled star) [33], fluid-crystal boundary (top right gray area) [34, 35], and the simulated RDG-ADG transition (top right solid lines) [35] which is shifted to higher ϕ based on prior experiments.[36] (b) For comparison, the dimensionless state diagram from the main text is shown in terms of the reduced second virial coefficient B_2^* and the interaction volume fraction η . Symbols and lines correspond to the descriptions above.

in Fig. 12 are the best-fit line for AHS (AR1), given by $\tau = m \log(V_p) + b$. Solids lines are extrapolated to larger V_p to compare between AHS and AHR.

For AHS, the average particle volume $V_p = \pi D^3/6$ is calculated using the particle diameter D of 28 ± 3 nm, 108 ± 11 nm, and 290 ± 29 nm, which are referred to as AR1 30 nm, AR1 100 nm, and AR1 300 nm, respec-

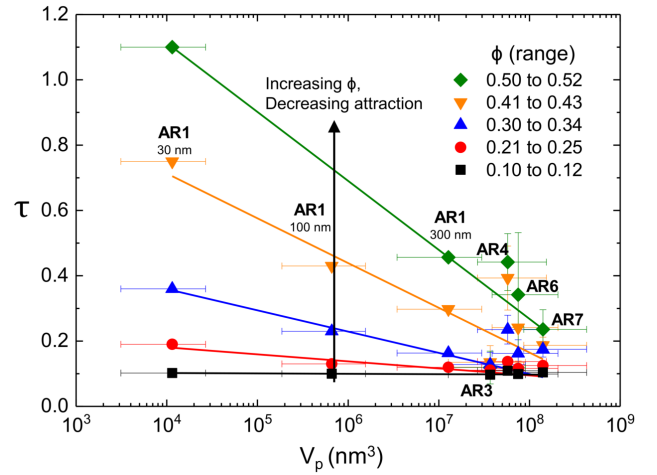


FIG. 12. The τ values are shown as a function of the average particle volume V_p . AHS systems are labeled as AR1 30 nm, AR1 100 nm, and AR1 300 nm [24, 25, 31]. AHR systems are labeled as AR3, AR4, AR6, and AR7 (this work). Samples are grouped into different ranges of ϕ , as shown in the legend. The solid lines correspond to the best-fit line for AHS systems, $\tau = m \log(V_p) + b$, which is extrapolated to higher V_p to compare with AHR systems.

tively [24, 25, 31]. For AHR, the average particle volume $V_p = \pi D^2 L/4$ was calculated using the average mean core diameter D and length L given in Table I. The higher and lower boundaries (x-error bars) are shown using ± 1 standard deviation in D and L .

At lower concentrations ($\phi < 0.2$), τ values for AHS and AHR are consistently within the range $\tau \approx 0.1 - 0.2$ and do not depend significantly on V_p . At higher concentrations ($\phi > 0.2$), a decrease in τ is generally correlated to an increase in V_p . There are exceptions to this general trend, for example, AR3 in the range $\phi = 0.41 - 0.52$, AR4 at $\phi = 0.32 - 0.52$, AR6 at $\phi = 0.32$, and AR7 at $\phi = 0.31$. In general, these deviations correspond to rod concentrations approaching or exceeding the hard rod glass boundary defined by ϕ_g for a given L/D .

- [1] R. P. Murphy, K. Hong and N. J. Wagner, *Langmuir*, 2016, **32**, 8424–35.
- [2] R. P. Murphy, K. Hong and N. J. Wagner, *J Colloid Interface Sci*, 2017, **501**, 45–53.
- [3] A. Kuijk, A. van Blaaderen and A. Imhof, *J. Am. Chem. Soc.*, 2011, **133**, 2346–2349.
- [4] H. H. Winter and F. Chambon, *J. Rheol.*, 1986, **30**, 367–382.
- [5] F. Chambon, Z. S. Petrovic, W. J. MacKnight and H. H. Winter, *Macromolecules*, 1986, **19**, 2146–2149.
- [6] P. N. Pusey and W. van Megen, *Phys. Rev. Lett.*, 1987, **59**, 2083–2086.
- [7] P. N. Pusey and W. van Megen, *Physica A*, 1989, **157**, 705–741.

- [8] W. van Meegen, S. M. Underwood and P. N. Pusey, *Phys. Rev. Lett.*, 1991, **67**, 1586–1589.
- [9] S. V. G. Menon, C. Manohar and K. S. Rao, *J. Chem. Phys.*, 1991, **95**, 9186–9190.
- [10] M. Doucet, J. H. Cho, G. Alina, J. Bakker, W. Bouwman, P. Butler, K. Campbell, M. Gonzales, R. Heenan, A. Jackson, P. Juhas, S. King, P. Kienzle, J. Krzywon, A. Markvardsen, T. Nielsen, L. O’Driscoll, W. Potrzebowski, R. Ferraz Leal, T. Richter, P. Rozycko, T. Snow and A. Washington, <http://www.sasview.org/>, Web, 2016, <http://www.sasview.org/>.
- [11] D. Chandler, R. Silbey and B. Ladanyi, *Molecular Physics*, 1982, **46**, 1335–1345.
- [12] K. S. Schweizer and J. G. Curro, *Advances in Polymer Science*, 1994, **116**, 319–377.
- [13] G. Yatsenko and K. S. Schweizer, *J. Chem. Phys.*, 2007, **126**, 014505.
- [14] R. Jadrach and K. S. Schweizer, *J. Chem. Phys.*, 2011, **135**, 234902.
- [15] G. Yatsenko and K. S. Schweizer, *Phys Rev E Stat Nonlin Soft Matter Phys*, 2007, **76**, 041506.
- [16] G. Yatsenko and K. S. Schweizer, *Langmuir*, 2008, **24**, 7474–7484.
- [17] R. Jadrach and K. S. Schweizer, *Phys Rev E Stat Nonlin Soft Matter Phys*, 2012, **86**, 061503.
- [18] M. Tripathy and K. S. Schweizer, *Phys Rev E Stat Nonlin Soft Matter Phys*, 2011, **83**, 041406.
- [19] M. Tripathy and K. S. Schweizer, *Phys Rev E Stat Nonlin Soft Matter Phys*, 2011, **83**, 041407.
- [20] R. P. Murphy, *PhD thesis*, University of Delaware, 2017.
- [21] R. J. Baxter, *J. Chem. Phys.*, 1968, **49**, 2770–2774.
- [22] Y. C. Chiew and E. D. Glandt, *J. Phys. A: Math. Gen.*, 1983, **16**, 2599–2608.
- [23] M. G. Noro and D. Frenkel, *J. Chem. Phys.*, 2000, **113**, 2941.
- [24] A. P. R. Eberle, R. Castaneda-Priego, J. M. Kim and N. J. Wagner, *Langmuir*, 2011, **28**, 1866–1878.
- [25] A. P. R. Eberle, N. J. Wagner and R. Castaneda-Priego, *Phys. Rev. Lett.*, 2011, **106**, 105704.
- [26] J. Ilavsky and P. R. Jemian, *J. Appl. Crystallogr.*, 2009, **42**, 347–353.
- [27] J. Ilavsky, P. R. Jemian, A. J. Allen, F. Zhang, L. E. Levine and G. G. Long, *J. Appl. Crystallogr.*, 2009, **42**, 469–479.
- [28] J. Ilavsky, *J. Appl. Crystallogr.*, 2012, **45**, 324–328.
- [29] H. W. Hatch, W. P. Krekelberg, S. D. Hudson and V. K. Shen, *J. Chem. Phys.*, 2016, **144**, 194902.
- [30] H. W. Hatch, N. A. Mahynski, R. P. Murphy, M. A. Blanco and V. K. Shen, *AIP Advances*, 2018, **8**, 095210.
- [31] J. M. Kim, J. Fang, A. P. R. Eberle, R. Castaneda-Priego and N. J. Wagner, *Phys. Rev. Lett.*, 2013, **110**, 208302.
- [32] N. E. Valadez-Pérez, Y. Liu, A. P. R. Eberle, N. J. Wagner and R. Castaneda-Priego, *Phys. Rev. E*, 2013, **88**, 060302(R).
- [33] M. A. Miller and D. Frenkel, *Phys. Rev. Lett.*, 2003, **90**, 135702.
- [34] D. W. Marr and A. P. Gast, *J. Chem. Phys.*, 1993, **99**, 2024–2031.
- [35] J. Bergholtz and M. Fuchs, *Phys. Rev. E*, 1999, **59**, 5706–5715.
- [36] K. N. Pham, A. M. Puertas, J. Bergholtz, S. Egelhaaf, A. Moussaid, P. N. Pusey, A. B. Schofield, M. E. Cates, M. Fuchs and W. C. K. Poon, *Science*, 2002, **296**, 104–106.